analytical chemistry

Article

Cite This: *Anal. Chem.* 2019, 91, 3374−3381

pubs.acs.org/ac

Nanoamplicon Comparator for Live-Cell MicroRNA Imaging

Min Huo,[†] Siqiao Li,[†] Peiwen Zhang, Yimei Feng, Yiran Liu, Na Wu, Huangxian Ju, and Lin Ding*

State Key Laboratory of Analytical Chemistry for Life Science, School of Chemistry and Chemical Engineering, Nanjing University, Nanjing 210023, PR China

Supporting Information

ABSTRACT: As an investigative tool, live-cell imaging requires superior probe design to guarantee imaging quality and data validity. The ability to simultaneously address the robustness, sensitivity, and consistency issues in a single-assay system is highly desired, but it remains a largely unsolved challenge. We describe herein a probe-design strategy called a nanoamplicon comparator (NAC) and demonstrate its proof-of-concept utility in intracellular microRNA (miRNA) imaging. This novel designer architecture builds upon spherical nucleic acids (SNAs) for robustness, catalytic hairpin assembly (CHA) for sensitivity, and upconversion nanoparticles (UNPs) for consistency. A catalytic circuit comprising a UNP−hairpin-DNA (UNP-HDNA) conjugate and a hairpin-DNA−organic-fluorophore (HDNA-F) conjugate as probe responds to target miRNA and generates the UNP-HDNA−HDNA-F complex as an NAC for quantitative UNP-to-organic-fluorophore-luminescence-resonance-energy-transfer (LRET) imaging against a native UNP-emission reference channel. An imaging application with miR21 shows the ability to monitor miRNA-expression levels across different cell lines and under an external stimulus.

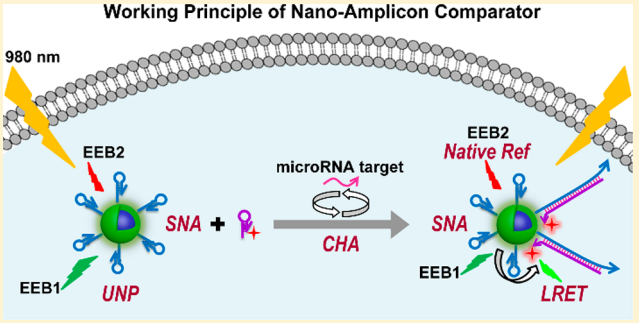

Live-cell imaging has emerged as a powerful tool for illuminating the structures and dynamics of biologically functional molecules.[1] Probe design is the dictating factor for imaging quality and data validity.[2] Key considerations for the development of an ideal probe include: robustness, sensitivity, and consistency. Robustness requires stability of the probe units, both before and after reacting with the target of interest. Sensitivity should be achieved in a target-specific-amplification manner while also involving minimal processing effort. Consistency implies the elimination of data fluctuation from altered imaging settings and the ability to perform quantitative analysis. Although it is apparently important, integration of all these desired assay attributes into a single probe system remains a largely unsolved challenge. We report herein a distinct type of designer-probe architecture, a nanoamplicon comparator (NAC), and demonstrate its proof-of-concept utility in live-cell imaging of microRNA (miRNA).

miRNAs are small, noncoding, endogenous RNAs that regulate gene expression and related biological processes.[3] Aberrant expression of miRNAs can lead to many disease states. The ability to detect intracellular miRNAs is therefore important for diagnosis, therapeutics, and drug screening.[4] The majority of methods developed thus far use hybridization-triggered fluorophore−quencher separation and fluorescence restoration for target signaling.[5−18] This fundamental principle has been implemented with a variety of different assay formats.[5−18] The hybridization event can occur either in solution[5−12] or on the surface,[13−18] and the signaling can be effected either stoichiometrically[5,7,8,13,14] or with amplification.[6,9−12,15−18] Despite the advances, all these protocols suffer from one or more drawbacks in the following assay attributes: lack of robustness as a result of the thermal instability of the solution-phase linear DNA strand as well as its susceptibility to intracellular-nuclease degradation (either originally in solution[5,7−11] or released into solution[13,14,16] after reacting with the target miRNA), limited sensitivity due to the use of a stoichiometric signaling event,[5,7,8,13,14] and inadequate consistency because of the absence of an internal reference.[5−18] Resorting to specially designed nucleic acid structures (e.g., peptide nucleic acids,[6] locked nucleic acids,[2] and phosphorothiolate-containing nucleic acids[12]) for increased thermal stability and nuclease resistance can impose significant restrictions on the application settings in view of synthesis costs, technical know-how, and commercial-availability problems. Requirement for enzymatic manipulation in certain protocols[9−11] can add another dimension of complexity and uncertainty to the assay process.

The above issues can be simultaneously addressed by taking advantage of three key probe-design elements, spherical nucleic acids (SNAs),[19] catalytic hairpin assembly (CHA),[20−23] and upconversion nanoparticles (UNPs),[24] thus leading to the proposal of NAC as an ideal tool for miRNA imaging (Figure 1). Basically, with miR21[25] as the proof-of-concept-demonstration target, a catalytic circuit comprising a UNP−hairpin-

Received: October 11, 2018
Accepted: February 8, 2019
Published: February 8, 2019

DOI: 10.1021/acs.analchem.8b04661
Anal. Chem. 2019, 91, 3374−3381

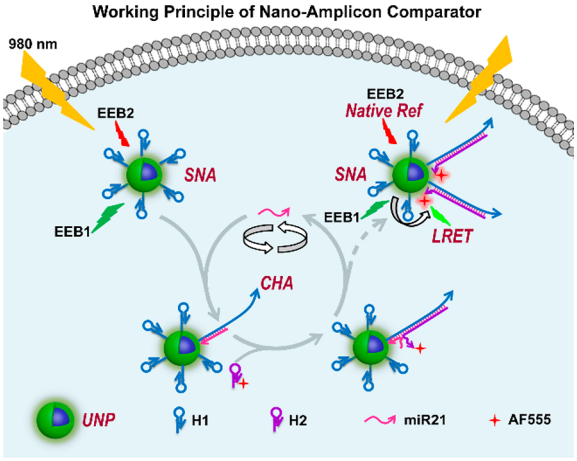

Figure 1. Schematic illustration of the working principle of NAC.

DNA (UNP-HDNA) conjugate UNP-H1 (all DNA sequences read from the 5′ end to the 3′ end) and a hairpin-DNA−organic-fluorophore (HDNA-F) conjugate H2-F (F = AF555) as probe responds efficiently to this highly conserved mammalian miRNA and important disease-state biomarker[25] and generates the NAC UNP-H1−H2-F complex, thus enabling the integration of three probe-design elements into a single imaging architecture: SNA, a distinct DNA construct on UNP that provides high binding strength and high nuclease resistance in both the original hairpin state and the subsequent duplex format (i.e., nano); multiple UNP-H1−H2-F complexes generated from one target miR21 by an enzyme-free, minimum-processing-required CHA turnover process (i.e., amplicon); and a UNP-to-AF555 luminescence-resonance-energy-transfer (LRET)-emission band as the signaling channel[24] and an intact UNP EEB2-emission band as the native reference channel (i.e., comparator). Unlike privileged-molecular-beacon (MB)[26] and nanoflare[27,28] technologies, the near-infrared excitation used in UNP-based system allows the elimination of otherwise interfering cellular-autofluorescence signals.[24] Collectively, all these desired assay attributes associated with NAC have given it the ability to monitor miRNA-expression levels across different cell lines and under external stimuli.

EXPERIMENTAL SECTION

Materials and Reagents. Rare-earth chlorides ($LnCl_3$, Ln = Y, Er, Gd, or Yb), sodium hydroxide, ammonium fluoride (NH_4F), cyclohexane, hexane, oleic acid (OA), 1-octadecene (ODE), nitrosonium tetrafluoroborate ($NOBF_4$), *N*-ethyl-*N*′-(3-(dimethylamino)propyl) carbodiimide hydrochloride (EDC), *N*-hydroxysulfosuccinimide sodium salt (sulfo-NHS), and poly(acrylic acid) (PAA) were purchased from Sigma-Aldrich Inc. Methanol, ethanol, 2-propanol, *N*,*N*-dimethylformamide (DMF), and acetone were obtained from Sinopharm Chemical Reagent Company, Ltd. TBE buffer (10×; containing 0.089 M Tris, 0.089 M boric acid, and 0.002 M EDTA) and 6× loading buffer were purchased from Shanghai Sangon Biotechnology Company, Ltd. UltraPower dye and Revert Aid First Strand cDNA Synthesis Kit (K1622) were purchased from Thermo Fisher Scientific Inc. Lipofectamine 3000 transfection reagent (Lipo-3000), 3-(4,5-dimethylthiazol-2-yl)-2-diphenyltetrazolium bromide (MTT), and Trizol Reagent were acquired from Invitrogen Company, Ltd. Deoxyribonuclease I (DNase I); fetal-bovine serum (FBS); trypsin; cell-culture media; phosphate-buffered saline (PBS; pH 7.4; containing 136.7 mM NaCl, 2.7 mM KCl, 8.72 mM Na_2HPO_4, 1.41 mM KH_2PO_4, 1 mM $CaCl_2$, and 1 mM $MgCl_2$); dimethyl sulfoxide (DMSO); and MDA-MB-231, HeLa, and MRC-5 cell lines were purchased from KeyGen Biotech Company, Ltd. Tris-HCl buffer (20 mM; pH 7.4; containing 20 mM Tris-HCl, 100 mM NaCl, 2 mM KCl, and 5 mM $MgCl_2$) was purchased from Beijing Leagene Biotechnology Company, Ltd. MicrOFF hsa-miR-21-5p antagomir reagent was purchased from Guangzhou Ribobio Company, Ltd. SYBR Green I RT-PCR Master Mix (QPK201) was purchased from Toyobo Inc. All of the chemicals used were of analytical grade. All aqueous solutions were prepared using ultrapure water (≥18 MΩ, Milli-Q, Millipore).

All DNA oligonucleotides were synthesized and purified using high-performance liquid chromatography either by Shanghai Sangon Biotechnology Company, Ltd. or Dalian Takara Biomedical Technology Company, Ltd. The miR21 mimics was synthesized and purified using high-performance liquid chromatography by Shanghai GenePharma Company, Ltd. All DNA and RNA sequences are listed in Table S1.

Apparatus. Transmission-electron-microscopy (TEM) images were obtained on a JEM-2100 transmission electron microscope (JEOL). Fourier-transform infrared (FT-IR) spectra were acquired on a Nicolet 6700 FT-IR Spectrometer (Thermo Fisher Scientific). Zeta-potential analysis was performed on a Zetasizer system (Nano-Z). UV−vis-absorption spectra were obtained with a UV-3600 UV−vis spectrophotometer (Shimadzu). Upconversion-luminescence (UCL) spectra were measured on a ZolixScan ZLX-UPL spectrometer with an external 980 nm laser as the excitation source. Fluorescence (FL) spectra were obtained on an RF-5301PC spectrofluorophotometer (Shimadzu). Polyacrylamide-gel-electrophoresis (PAGE) analysis was performed on an electrophoresis analyzer (Bio-Rad) and imaged on a Bio-Rad ChemiDoc XRS system (Bio-Rad). UV−vis absorbance for the MTT assay was obtained on a spectral-scanning multimode reader (Thermo Fisher Scientific). Cell images were obtained on a TCS SP5 confocal laser-scanning microscope (CLSM, Leica). Quantitative reverse-transcription polymerase chain reaction (qRT-PCR) was performed with a StepOnePlus RT-PCR system (ABI).

Preparation of H1-Conjugated Core−Shell $NaYF_4$:Er/Gd/Yb@$NaGdF_4$ UNP (UNP-H1). To a 200 μL PBS solution of PAA-modified core−shell $NaYF_4$:Er/Gd/Yb@$NaGdF_4$ UNP (PAA-UNP, 1 mg/mL, 33 nM) were added EDC (15.3 mg, final concentration of 0.4 μM) and sulfo-NHS (4.34 mg, final concentration of 0.1 μM). The reaction was allowed to proceed at room temperature (rt) for 4 h. Then, excess EDC and sulfo-NHS were washed away by centrifugation, and the carboxyl-activated PAA-UNP was obtained. The carboxyl-activated PAA-UNP was then dispersed in 200 μL of PBS solution and mixed with 20 μL of an ultrapure water solution of H1 (100 μM). The reaction was allowed to proceed at rt under vibration for 3 h. The as-prepared UNP-H1 was subsequently centrifugally washed several times with PBS.

PAGE Analysis. A 200 μL Tris-HCl buffer solution containing hairpin-DNA pairs (100 μM each) was annealed over a temperature gradient from 95 to 25 °C. A 7 μL DNA sample along with 1.5 μL of 6× loading buffer and 1.5 μL of UltraPower dye was then loaded onto a 12% polyacrylamide hydrogel in 1× TBE buffer. Electrophoresis was allowed to run

DOI: 10.1021/acs.analchem.8b04661
Anal. Chem. 2019, 91, 3374−3381

at 110 V in TBE buffer for 1 h. The DNA bands were illuminated with UV light and photographed with a Molecular Imager Gel Doc XR.

In Vitro Experiments. For the LRET process involving the UNP used herein, an ideal acceptor fluorophore is AF555. Therefore, all the LRET experiments were performed with AF555. FAM was employed in plain hairpin-hybridization experiments as it allows, when used in conjunction with the quencher DABCYL, convenient monitoring of the hairpin opening of H1 and H2.

For fluorescence experiments, the concentrations of FAM-H1-Q, H2, and miR21-D were 50, 150, and 5 nM, respectively. After incubation of the mixture at 37 °C for 2 h, the fluorescence of FAM was monitored. The excitation wavelength was set to 480 nm and emission spectrum was measured from 490 to 600 nm in 1 nm increments.

For the UCL experiments, the concentrations of UNP-H1, H2-F, and miR21-D were 300 μg/mL (10 nM), 300 nM, and 100 nM, respectively. The mixture was first incubated at 37 °C for 3 h, and then excess reagents in the supernatant were removed through centrifugation at 6000 rpm. The I_{LRET}/I_{EEB2} value (peak signal intensity used; λ_{ex} = 980 nm; λ_{em} = 572 nm for LRET; λ_{em} = 656 nm for EEB2) could then be obtained from the UCL spectrum.

For monitoring the time-dependent CHA turnover process (amplification time course), the concentration of UNP-H1 used was either 1 or 10 nM; the concentrations of miR21-D-FAM and miR21-D were identical and could be 10, 50, or 100 nM; the concentration of H2-FAM was 300 nM. The calibration curves for miR21-D-FAM and H2-FAM were obtained using the 518 nm peak signal intensity (λ_{ex} = 485 nm). For the stoichiometric binding experiment, after incubation of a PBS solution of UNP-H1 and miR21-D-FAM for different time durations, the hybridized complex was centrifugally washed twice (6 min each time) at 10 000 rpm with PBS buffer. The hybridized complex was redispersed in PBS, and the fluorescence of FAM was measured. For the CHA experiment, the experimental procedure was otherwise identical except for the replacement of the PBS solution of UNP-H1 and miR21-D-FAM with a PBS solution of UNP-H1, H2-FAM, and miR21-D.

For the sensitivity and dynamic-range experiment, the concentrations of UNP-H1 and H2-F used were 300 μg/mL (10 nM) and 300 nM, respectively. After the incubation of a PBS solution of UNP-H1, H2-F, and miR21-D (different concentrations) for 3 h, the I_{LRET}/I_{EEB2} value (peak signal intensity used; λ_{ex} = 980 nm; λ_{em} = 572 nm for LRET; λ_{em} = 656 nm for EEB2) was obtained from the UCL spectrum. For the specificity experiments, all DNA analogues of miRNA were prepared at concentrations of 20 nM.

Investigation of Nuclease Stability. Three experiments were carried out to evaluate the nuclease stability of UNP-H1 and the UNP-H1−H2-F complex by monitoring the change of LRET intensity. In the first experiment, a PBS solution of UNP-H1-F was diluted to a final concentration of 300 μg/mL (10 nM), and the mixture was allowed to stand with and without DNase I (50 U/mL DNase I, final concentration of 50 U/L). In the second experiment, UNP-H1 (10 nM) and H2-F (300 nM) were allowed to stand with and without DNase I (50 U/mL DNase I, final concentration of 50 U/L). In the third experiment, UNP-H1 (10 nM), H2-F (300 nM), and miR21-D (100 nM) were incubated at 37 °C for 3 h, and the mixture was allowed to stand with and without DNase I (50 U/mL DNase I, final concentration of 50 U/L). The LRET intensity was monitored in 2 h intervals for 6 h.

Cell Culturing and Cytotoxicity Assay. The HeLa and MRC-5 cells were cultured in Dulbecco's modified Eagle's medium (DMEM, Gibco) supplemented with 10% FBS, penicillin (100 μg/mL), and streptomycin (100 μg/mL) at 37 °C in a humidified chamber containing 5% CO_2. The MDA-MB-231 cells (ATCC) were grown in relevant media (Leibovitz's L-15 medium) supplemented with 10% FBS, penicillin (100 μg/mL), and streptomycin (100 μg/mL) at 37 °C in a humidified chamber containing 5% CO_2.

The cytotoxicity of PAA-UNP and UNP-H1 was examined by an MTT assay. After MDA-MB-231 cells (100 μL, 1.0×10^4 cells/mL) were seeded in the wells of a 96-well plate for 12 h, the medium was discarded. The cells were then washed twice with PBS and incubated with 100 μL of culture medium containing either PAA-UNP or UNP-H1 of different concentrations (0, 0.1, 0.2, 0.3, 0.4, 0.5, and 0.6 mg/mL) for 24 h. After the medium was discarded, and the cells were washed with PBS, MTT (50 μL, 1 mg/mL) was added to each well, and the mixture was incubated at 37 °C for 4 h to allow the formation of formazan. Then 100 μL of DMSO was added to each well, and the cell plate was vibrated at rt for 15 min to dissolve the formazan. Finally, the absorbance of each well was measured at 490 nm on a microplate reader. The relative cell viability (%) was calculated by $(A_{test} - A_{blank})/(A_{control} - A_{blank}) \times 100\%$. The culture medium was used as the blank, and cells incubated in culture medium without PAA-UNP and UNP-H1 were used as the control.

Liposome Transfection. In one reaction vessel, a 45 μL PBS solution of UNP-H1 (1 mg/mL, 33 nM) and a 0.45 μL ultrapure water solution of H2-F (100 μM) were mixed with 55 μL of serum-free medium and incubated for 5 min. In the other reaction vessel, 0.75 μL of Lipo-3000 was dissolved in 50 μL of serum-free medium and also incubated for 5 min. The two solutions were mixed and incubated at 37 °C for 15 min, which led to the coencapsulation of both UNP-H1 and H2-F in Lipo-3000. Then, the mixture was incubated with the cells of interest for 6 h. The cells were washed three times with serum-free medium before being imaged by CLSM.

Aptamer Delivery. As an alternative to Lipo-3000 transfection, H2-F delivery can be achieved through conjugation with a cell-recognition aptamer[29−31] (as Apt−H2-F). Briefly, a 45 μL PBS solution of UNP-H1 (1 mg/mL, 33 nM) and a 0.9 μL PBS solution of Apt−H2-F (100 μM) were mixed with 105 μL of serum-free medium and incubated for 5 min. Then, the mixture was incubated with the cells of interest at 37 °C for 6 h. The cells were washed three times with serum-free medium before being imaged by CLSM.

CLSM Analysis. The MDA-MB-231, HeLa, and MRC-5 cells were separately seeded on four-well confocal dishes and cultured in a 37 °C, 5% CO_2 incubator for 12 h. After being washed three times with PBS to remove the culture medium, the cells were incubated with the Lipo-3000 mixture containing 300 μg/mL (10 nM) UNP-H1 and 300 nM H2-F for 6 h. The cells were carefully washed twice with PBS and then immediately imaged with CLSM. The UCL signal was collected by CLSM under 980 nm excitation, with the EEB1-, LRET-, and EEB2-channel signals collected in the 530−560, 562−600, and 640−670 nm ranges, respectively. The AF555 signal was obtained by CLSM under 514 nm excitation with a collection range of 562−600 nm. The average I_{LRET}/I_{EEB2} value

DOI: 10.1021/acs.analchem.8b04661
Anal. Chem. 2019, 91, 3374−3381

was obtained by the CLSM software from 10 individual cells from three parallel experiments for each cell.

Inhibition Assay. The MDA-MB-231 cells were seeded on three four-well confocal dishes and cultured in a 37 °C, 5% CO_2 incubator for 12 h. After being washed three times with L-15 medium, the cells in two of the dishes were treated with 50 and 100 nM micrOFF hsa-miR-21-5p antagomir in L-15 medium, whereas the cells in the other dish were not treated. After incubating for 24 h and being washed three times with L-15 medium, the cells in the three dishes underwent transfection with Lipo-3000 containing UNP-H1 and H2-F for 6 h before being imaged with CLSM. The inhibition assay for HeLa cells was performed analogously with 100 nM micrOFF hsa-miR-21-5p antagomir.

Assessment of miR21-Expression Levels with miR21 Mimics. The MDA-MB-231 cells were separately seeded on four-well confocal dishes and cultured in a 37 °C, 5% CO_2 incubator for 12 h. After being washed three times with PBS to remove culture medium, the cells (~6390) were cultured with the Lipo-3000 mixture containing 6, 12, 18, 24, or 30 nM miR21 mimics (100 μL; corresponding to 1.25, 2.50, 3.75, 5.00, and 6.25 pg/cell, respectively; molecular weight of 13.3 kDa) for another 24 h. The cells were then incubated with the Lipo-3000 mixture containing 10 nM UNP-H1 and 300 nM H2-F for 6 h. The cells were carefully washed twice with PBS and then immediately imaged with CLSM. The average I_{LRET}/I_{EEB2} value was obtained by the CLSM software from five individual cells.

RESULTS AND DISCUSSION

Fabrication and Characterization of the Probe. With the NAC architecture being well-designed, we started the fabrication of UNP-H1 and the H2-F probe. The highly luminescent core−shell UNP employed herein, $NaYF_4$:Er/Gd/Yb@$NaGdF_4$ (26 nm, Figure S1A),[32] was initially synthesized in the OA-capping format. This hydrophobic OA-UNP was then, through ligand exchange with PAA, transformed into hydrophilic PAA-UNP (Figure S1A).[32] Infrared spectroscopy (attenuation of the peak intensity for the asymmetrical stretching mode of the $-CH_2-$ group at 2956 cm^{-1}, Figure S1B) and zeta-potential measurements (from +43.5 to −30.6 mV, Figure S1C) confirmed the occurrence of ligand exchange. Conjugation of a 5′-amino-functionalized HDNA, H1, to carboxylic acid rich PAA-UNP was effected, as confirmed by the appearance of a 260 nm absorption band (Figure S1D), through *N*-ethyl-*N*′-(3-(dimethylamino)propyl)carbodiimide−*N*-hydroxysulfo-succinimide activation chemistry, affording the assay-ready UNP-H1 unit. This conjugation process is also accompanied by a change of the zeta potential to −11.5 mV (Figure S1C). The loading density of H1 on UNP is estimated to be 74 H1 strands per UNP (Figure S2). UNP-H1 exhibits essentially identical emission properties to those of PAA-UNP (Figure S1E) under 980 nm excitation. The sitting of two sharp bands (EEB1, 530−560 nm; EEB2, 640−670 nm) on virtually zero spectral baseline renders UNP-H1 ideally suited for the achievement of a high signal-to-noise ratio. The other assay unit, H2-F, was designed by placing a fluorophore, AF555 (562−600 nm fluorescence under 514 nm excitation), at the 3′ end of the HDNA. Thus, the overlap of the AF555-absorption band with the EEB1-emission band is expected to switch the LRET signal (i.e., AF555 emission under 980 nm excitation: 562−600 nm) from "off" to "on" in the presence of miR21. Fluctuations in the imaging settings, such as that in the incident laser intensity, can be corrected by using the EEB2-emission band as the native reference. In practice, the I_{LRET}/I_{EEB2} value is taken as the working parameter for quantitative analysis of miRNA.

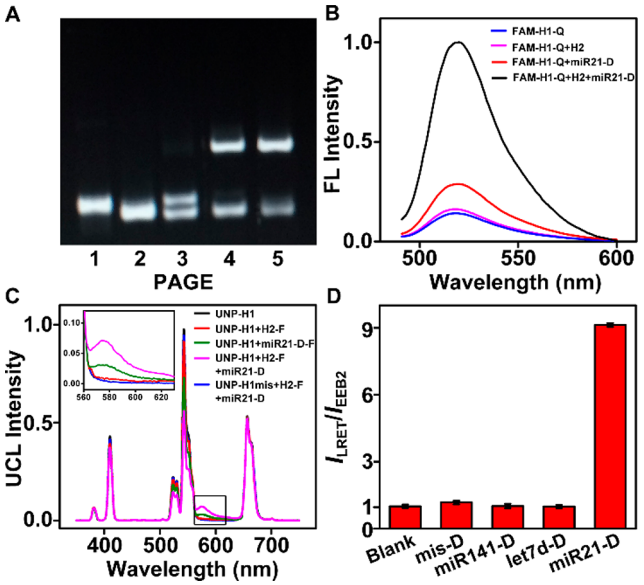

Figure 2. Demonstration of the feasibility of using NAC for in vitro sequence-specific identification of miR21. (A) PAGE electropherogram for monitoring the CHA process. Lanes 1−5: H1; H2; H1 and H2 at rt; H1 and H2 after annealing from 95 °C; H1, H2, and miR21-D at rt. (B) Fluorescence spectra of FAM-H1-Q in the absence and presence of H2 and miR21-D. (C) Upconversion luminescence spectra of UNP-H1 alone and of UNP-H1 in the presence of H2-F only, miR21-D-F only, and both H2-F and miR21-D. Also employed for comparison is a sample containing UNP-H1mis, H2-F, and miR21-D. Inset: magnified view of the LRET region. (D) I_{LRET}/I_{EEB2} values (peak signal intensity used; λ_{em} = 572 nm for LRET; λ_{em} = 656 nm for EEB2; normalized against the blank sample) in the presence of different DNA sequences.

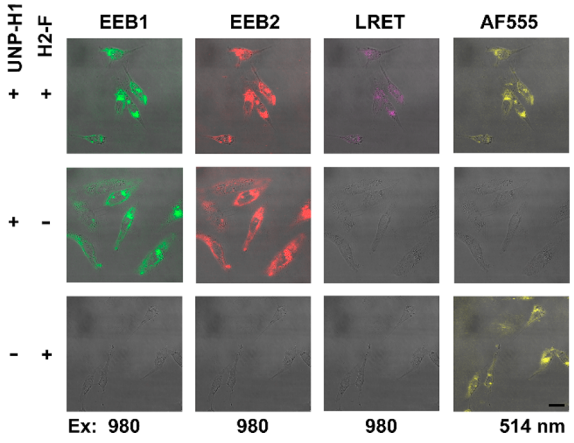

Figure 3. Demonstration of the feasibility of using NAC for live-cell imaging of miR21. CLSM images of MDA-MB-231 cells after incubation for 6 h in the absence and presence of 10 nM UNP-H1 and 300 nM H2-F (in a Lipo-3000 formulation). Scale bar: 25 μm.

Demonstration of the Feasibility of the CHA Reaction. The feasibility of the CHA reaction for the designed sequences was initially assessed by using a DNA analogue[2,13] of miR21, miR21-D, as the prospective pseudotarget. The two complementary HDNA strands, H1

DOI: 10.1021/acs.analchem.8b04661
Anal. Chem. 2019, 91, 3374−3381

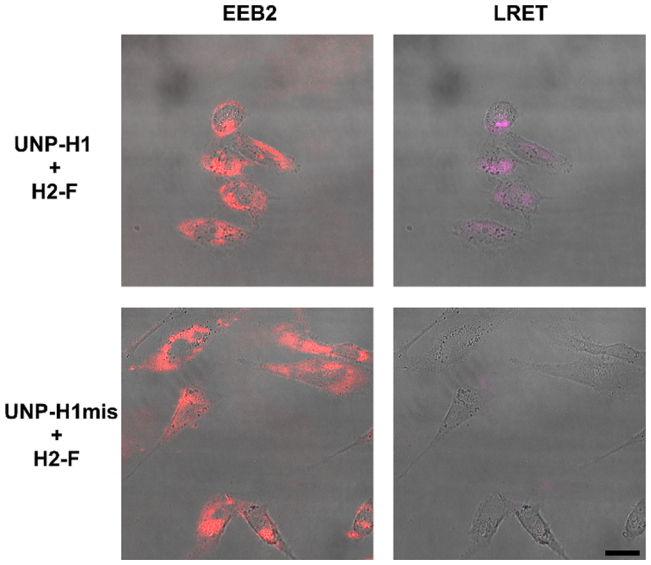

Figure 4. Demonstration of miR21-target-imaging specificity using the NAC. CLSM images of MDA-MB-231 cells after incubation with UNP-H1 and H2-F (top) or with UNP-H1mis and H2-F (bottom). Scale bar: 25 μm.

and H2, are kinetically trapped at room temperature (Figure 2A, lane 3) but can hybridize efficiently under high-temperature annealing conditions (Figure 2A, lane 4), as can be observed by PAGE. The same hybridization efficiency can be achieved under CHA conditions, with miR21-D as the catalytic reagent (Figure 2A, lane 5). Further verification of the feasibility of the CHA reaction comes from fluorescence-recovery experiments on an MB (Figure 2B). The MB molecule FAM-H1-Q (Q = DABCYL) exhibits minimum fluorescence emission in the absence and presence of H2. The fluorescence can be partly restored upon the mixing of FAM-H1-Q with miR21-D, signifying the opening of the MB. Further addition of H2 allows the occurrence of miR21-D turnover and full operation of the catalytic circuit, resulting in a significantly increased fluorescence intensity. The effectiveness of the solution-phase probe system prompts evaluation of the competency of UNP-H1, with HDNA in the surface-bound state, for the CHA reaction. In contrast to the unquenched background-fluorescence signal frequently observed for MB systems (Figure 2B), essentially zero background signal is identified for a solution containing UNP-H1 and H2-F (Figure 2C). Challenge of UNP-H1 with miR21-D-F leads to the emergence of an LRET peak. A more prominent LRET peak shows up with the introduction of both UNP-H1 and H2-F into the miR21-D solution. Under all these conditions, the EEB2-emission band remains intact against the influence of other emission bands (EEB1 and LRET), suggesting its capability of being used as the native reference channel. Additional evidence for the occurrence of CHA turnover is derived from a quantitative comparison of the stoichiometric binding kinetics of UNP-H1 with miR21-D-FAM and the CHA kinetics of UNP-H1, H2-FAM, and miR21-D (Figures S3 and S4, as well as the kinetic analysis based on the quasi-steady-state approximation and numerical simulation). Amplification is more pronounced at lower miR21-D concentrations, thus ensuring the ability to achieve sensitive analysis. Because of the likely complicated involvement of diverse DNA intermediates and metastable states[33−36] as well as DNA-

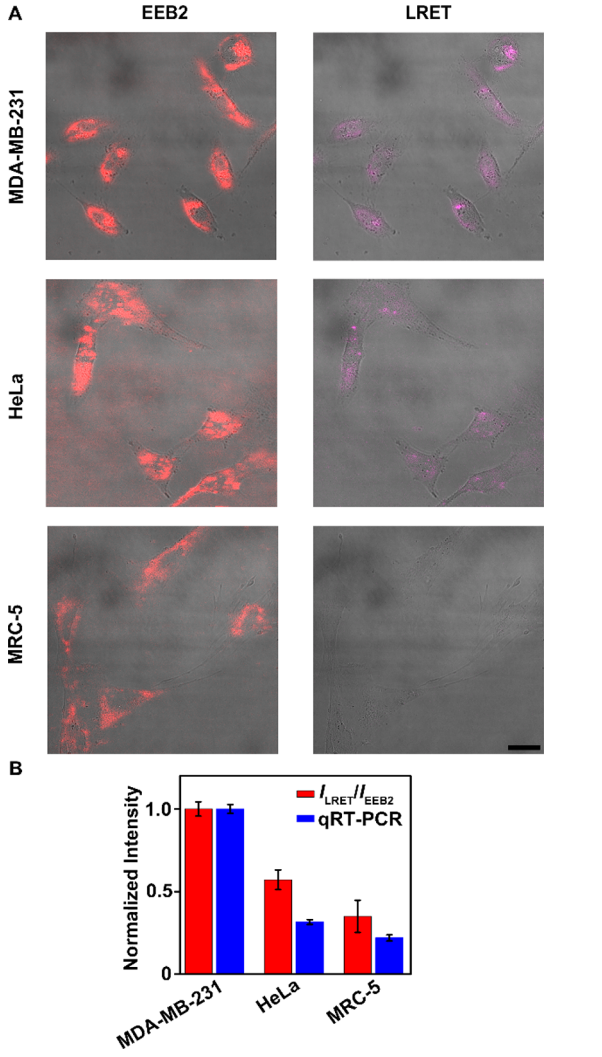

Figure 5. Quantitative analysis of miR21-expression levels across different cell lines. (A) CLSM images of MDA-MB-231, HeLa, and MRC-5 cells after incubation with UNP-H1 and H2-F. Scale bar: 25 μm. (B) Quantitative analysis of miR21-expression levels through CLSM imaging and qRT-PCR. Normalization is performed against MDA-MB-231 cells.

diffusion dynamics,[37] a full account of the mechanistic pathways requires further systematic studies. A detection limit (3σ method) of 1.02 nM and a linear dynamic range of 10−200 nM can be realized for miR21-D in vitro with 10 nM UNP-H1 and 300 nM H2-F probe (Figure S5). The high selectivity associated with the CHA process can translate to selectivity in the differentiation of complementary strands from noncomplementary ones.[20−23] Indeed, a background-level signal is observed when using the control probe unit UNP-H1mis (Figure 2C), which bears a mismatched DNA sequence, H1mis, against miR21-D. For further confirmation of the selectivity, the responsiveness of UNP-H1 and H2-F to a series of different DNA sequences, including mismatched mis-D, highly homologous miR141-D, and let7d-D, was examined (Figure 2D). Again, background-level I_{LRET}/I_{EEB2} values were invariably observed. Taken together, these experiments have established the effectiveness of using NAC for in vitro sequence-specific identification of target.

Nuclease Stability and Biocompatibility of the Probe. Before proceeding to the intracellular imaging of miR21, the

DOI: 10.1021/acs.analchem.8b04661
Anal. Chem. 2019, 91, 3374−3381

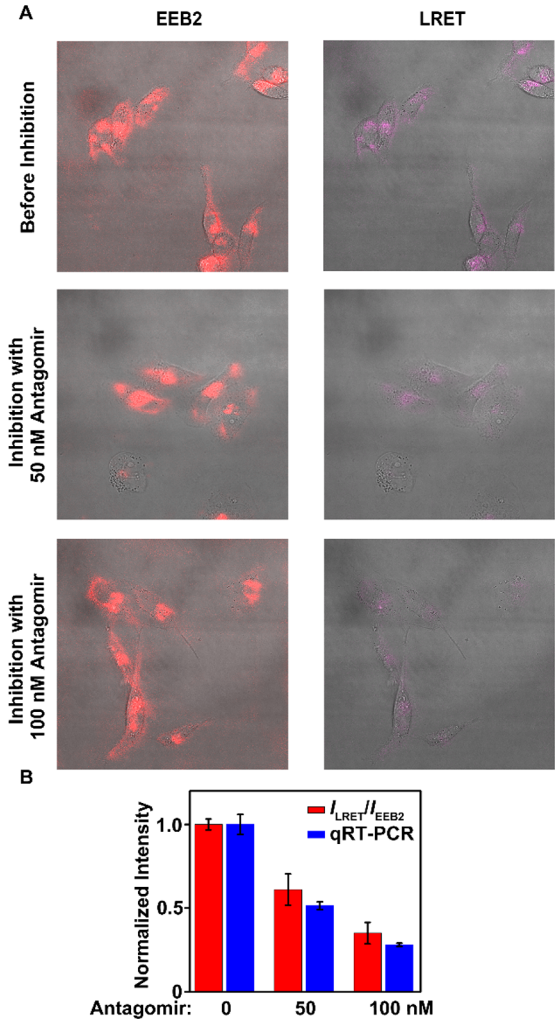

Figure 6. Quantitative monitoring of miR21-expression levels under antagomir inhibition in MDA-MB-231 cells. (A) CLSM images of cells before and after inhibition with 50 and 100 nM antagomir. Scale bar: 25 μm. (B) Quantitative analysis of miR21-expression levels through CLSM imaging and qRT-PCR. Normalization is performed against cells before inhibition.

nuclease stabilities of the UNP-H1 probe and the UNP-H1–H2-F complex were first evaluated (Figure S6). High stability is evidenced by the negligible reduction in LRET signal under DNase I treatment for both a sample containing UNP-H1-F and a sample containing UNP-H1, H2-F, and miR21-D.[19] Superior to the MB design, the NAC architecture can also protect against false-positive readouts even in the occurrence of accidental-degradation events. For example, the distance-dependent LRET process ensures that, even if H2-F could be partially cleaved by intracellular enzymes, no LRET signal would be generated. In addition, the hairpin design of the H2-F probe contributes to its heightened resistance against enzymatic degradation. High cell viability is observed through the MTT assay, which involved prolonged incubation of miR21-expressing MDA-MB-231 cells with PAA-UNP or UNP-H1 (Figure S7), demonstrating the biocompatibility of UNP-H1.

NAC-Based miRNA Imaging. Examination of the cellular-internalization capability of UNP-H1 shows that although UNP-H1 can directly enter cells (Figure S8, EEB2 channel), as confirmed by CLSM, Lipo-3000 enables more efficient delivery (Figures S9–S11, EEB2 channel). Also, recognizing the required use of Lipo-3000 for the cellular uptake of H2-F (Figure S8, no signal observed for the AF555 channel), this cationic reagent is deployed for the transfection of both UNP-H1 and H2-F. The high transfection efficacy of Lipo-3000 allows the use of NAC for miR21 imaging (Figure 3). The signal of the LRET channel depends on both probe concentration (Figure S9) and incubation time (Figure S10), and extensive optimization of these experimental parameters resulted in a probe concentration of 10 nM UNP-H1 and 300 nM H2-F and an incubation time of 6 h. Indeed, the participation of both UNP-H1 and H2-F permits simultaneous observation of four spatially colocalized signals (EEB1, EEB2, LRET, and AF555 fluorescence; Figure 3, top), verifying that the miR21-signaling LRET process originates from the UNP–AF555 pair. In the exclusive presence of either UNP-H1 or H2-F, only the corresponding UNP luminescence signal (EEB1 and EEB2; Figure 3, middle) or AF555 fluorescence signal (Figure 3, bottom) can be identified, and the LRET signal is considered completely off. The specificity of the target response is confirmed by the vastly reduced LRET signal with the replacement of UNP-H1 by UNP-H1mis (Figure 4). The CHA turnover process can be observed, on the basis of the time-course evolution of the LRET and EEB2 signals, after the incubation of the cells with UNP-H1 and H2-F for 3 h and beyond (Figure S11). It should be noted that H2-F delivery can be alternatively achieved through conjugation with a cell-recognition aptamer[29,30] (such as Apt–H2-F), which in combination with direct cellular internalization of UNP-H1 enables the elimination of Lipo-3000 and permits more convenient imaging of miRNA (Figure S12).

Quantitative Analysis of miRNA-Expression Levels. The I_{LRET}/I_{EEB2} value provides a reliable working parameter under varied imaging settings, as demonstrated in Figure S13. The I_{LRET} and I_{EEB2} values apparently vary with changes in laser intensity, whereas the I_{LRET}/I_{EEB2} value is more reliable as the working parameter because fluctuation in the laser intensity does not affect the readout, thus guaranteeing batch-to-batch consistency in the readout. This should allow quantitative analysis of miRNA-expression levels across different cell lines and under external stimuli. To test this, MDA-MB-231, HeLa (Figure S14), and MRC-5 (Figure S15) cells were challenged with UNP-H1 and H2-F. The three cell lines exhibit distinct LRET signal intensities when compared against the EEB2 native reference (Figure 5A), suggesting differences in miR21-expression levels. In support of this, the I_{LRET}/I_{EEB2} values correlate well with those obtained from qRT-PCR (Figure 5B), indicating that NAC can indeed serve as a quantitative miRNA-imaging tool. The copy number of miR21 in a single HeLa cell has been determined to be 24 496.[38] The I_{LRET}/I_{EEB2} value for HeLa cells is 0.57 when the I_{LRET}/I_{EEB2} value for MDA-MB-231 cells is normalized to 1 (Figure 5). The copy number of miR21 in a single MDA-MB-231 cell is therefore determined to be ~43 000.

Effect of Antagomir Inhibition on miRNA-Expression Levels. The quantitative-analysis ability is also corroborated by an antagomir[39] inhibition experiment. The LRET signal undergoes a marked decrease after the silencing of miR21 in MDA-MD-231 cells by an anti-miR21 antagomir (Figure 6A). Again, qRT-PCR confirms the validity of the quantitative I_{LRET}/I_{EEB2} results (Figure 6B). A similar inhibition effect can be identified in HeLa cells through both the I_{LRET}/I_{EEB2} and qRT-PCR readouts (Figure S16). Further assessment of

DOI: 10.1021/acs.analchem.8b04661
Anal. Chem. 2019, 91, 3374–3381

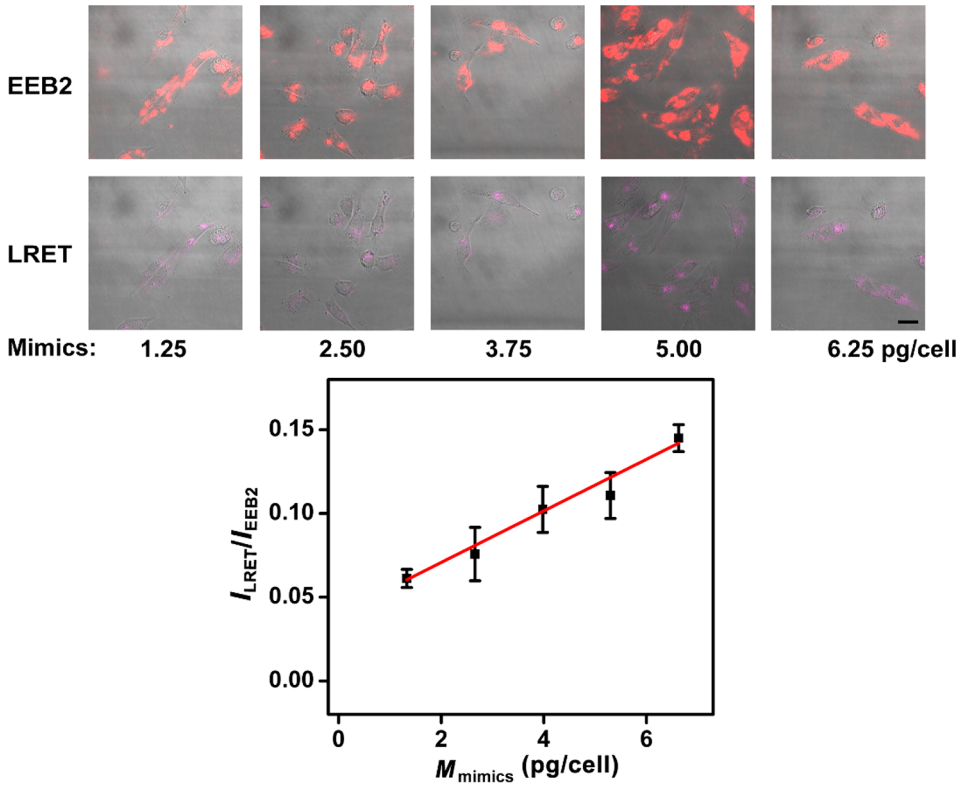

Figure 7. Assessment of miR21-expression levels using miR21 mimics. Top: CLSM images of MDA-MB-231 cells after initial incubation with a Lipo-3000 formulation containing miR21 mimics of different quantities for 24 h and subsequent incubation with a Lipo-3000 formulation containing 10 nM UNP-H1 and 300 nM H2-F at 37 °C for 6 h. Scale bar: 25 μm. Bottom: I_{LRET}/I_{EEB2} value as a function of miR21-mimic quantity.

miR21-expression levels by performing standard addition analysis on cells (MDA-MB-231) with varied amounts of a miR21 mimics (Figure 7) gives an average-miR21-quantity equivalent of 2.5 pg of miR21 mimics per cell (i.e., 1.13×10^8 copies). The functional internalization efficiency, defined as the percentage of internalized miR21 from miR21 mimics, is calculated as being $43\,000/(1.13 \times 10^8) = 0.038\%$. The I_{LRET}/I_{EEB2} value extrapolated to the point of no miR21 mimics (Figure 7) is essentially identical to the direct readout (Figure S10), further validating the effectiveness of our imaging protocol. Collectively, besides being equally effective as a quantitative-analysis tool, the NAC architecture can also provide in situ spatial−temporal information that is unattainable with qRT-PCR.

CONCLUSION

In summary, we have proposed herein a probe-design concept termed NAC and demonstrated its utility in live-cell miRNA imaging. A catalytic circuit comprising UNP-HDNA and HDNA-F responds to target miRNA and generates NAC for LRET readout against a native EEB2 reference channel. Robustness, sensitivity, and consistency are the key assay attributes, and they have been simultaneously addressed in this novel designer-probe architecture. The modularity of the catalytic circuitry should permit its ready adaptation to assays of wide-ranging targets in diverse biological contexts.

ASSOCIATED CONTENT

Supporting Information

The Supporting Information is available free of charge on the ACS Publications website at DOI: 10.1021/acs.analchem.8b04661.

DNA- and RNA-sequence information, characterization details of UNP, calculation of H1 loading density on UNP, CHA kinetics, in vitro sensitivity and dynamic range of NAC, stability of the NAC against DNase I, cytotoxicity assessment, necessity of Lipo-3000, optimization of concentration and incubation time, time-course evolution of LRET and EEB2, in vivo fluorescence images, advantages of using I_{LRET}/I_{EEB2} as the working parameter, and quantitative monitoring of miR21-expression levels (PDF)

AUTHOR INFORMATION

Corresponding Author

*Tel. and Fax: +86-25-89681927. E-mail: dinglin@nju.edu.cn.

ORCID

Huangxian Ju: 0000-0002-6741-5302

Lin Ding: 0000-0001-5381-3484

Author Contributions

†M.H. and S.L. contributed equally to this work

Notes

The authors declare no competing financial interest.

ACKNOWLEDGMENTS

We gratefully acknowledge support from the National Natural Science Foundation of China (21675082 and 21635005), the

DOI: 10.1021/acs.analchem.8b04661
Anal. Chem. 2019, 91, 3374−3381

National Basic Research Program of China (2014CB744501), and the State Key Laboratory of Analytical Chemistry for Life Science (5431ZZXM1801).

REFERENCES

(1) Kowada, T.; Maeda, H.; Kikuchi, K. *Chem. Soc. Rev.* **2015**, *44*, 4953−4972.
(2) Wu, C.; Cansiz, S.; Zhang, L.; Teng, I. T.; Qiu, L.; Li, J.; Liu, Y.; Zhou, C.; Hu, R.; Zhang, T.; Cui, C.; Cui, L.; Tan, W. *J. Am. Chem. Soc.* **2015**, *137*, 4900−4903.
(3) Carthew, R. W.; Sontheimer, E. J. *Cell* **2009**, *136*, 642−655.
(4) Bracken, C. P.; Scott, H. S.; Goodall, G. J. *Nat. Rev. Genet.* **2016**, *17*, 719−732.
(5) Kang, W. J.; Cho, Y. L.; Chae, J. R.; Lee, J. D.; Choi, K.-J.; Kim, S. *Biomaterials* **2011**, *32*, 1915−1922.
(6) Sadhu, K. K.; Winssinger, N. *Chem. - Eur. J.* **2013**, *19*, 8182−8189.
(7) Kang, W. J.; Cho, Y. L.; Chae, J. R.; Lee, J. D.; Ali, B. A.; Al-Khedhairy, A. A.; Lee, C. H.; Kim, S. *Biomaterials* **2012**, *33*, 6430−6437.
(8) Kim, J. K.; Choi, K.-J.; Lee, M.; Jo, M.-h.; Kim, S. *Biomaterials* **2012**, *33*, 207−217.
(9) Deng, R.; Tang, L.; Tian, Q.; Wang, Y.; Lin, L.; Li, J. *Angew. Chem., Int. Ed.* **2014**, *53*, 2389−2393.
(10) Xu, J.; Wu, Z.-S.; Wang, Z.; Le, J.; Zheng, T.; Jia, L. *Biomaterials* **2017**, *120*, 57−65.
(11) Min, X.; Zhang, M.; Huang, F.; Lou, X.; Xia, F. *ACS Appl. Mater. Interfaces* **2016**, *8*, 8998−9003.
(12) Cheglakov, Z.; Cronin, T. M.; He, C.; Weizmann, Y. *J. Am. Chem. Soc.* **2015**, *137*, 6116−6119.
(13) Choi, C. K. K.; Li, J.; Wei, K.; Xu, Y. J.; Ho, L. W. C.; Zhu, M.; To, K. K. W.; Choi, C. H. J.; Bian, L. *J. Am. Chem. Soc.* **2015**, *137*, 7337−7346.
(14) Dong, H.; Lei, J.; Ju, H.; Zhi, F.; Wang, H.; Guo, W.; Zhu, Z.; Yan, F. *Angew. Chem., Int. Ed.* **2012**, *51*, 4607−4612.
(15) Li, L.; Feng, J.; Liu, H.; Li, Q.; Tong, L.; Tang, B. *Chem. Sci.* **2016**, *7*, 1940−1945.
(16) Liu, H.; Tian, T.; Ji, D.; Ren, N.; Ge, S.; Yan, M.; Yu, J. *Biosens. Bioelectron.* **2016**, *85*, 909−914.
(17) He, X.; Zeng, T.; Li, Z.; Wang, G.; Ma, N. *Angew. Chem., Int. Ed.* **2016**, *55*, 3073−3076.
(18) Peng, H.; Li, X.-F.; Zhang, H.; Le, X. C. *Nat. Commun.* **2017**, *8*, 14378−14390.
(19) Cutler, J. I.; Auyeung, E.; Mirkin, C. A. *J. Am. Chem. Soc.* **2012**, *134*, 1376−1391.
(20) Jung, C.; Allen, P. B.; Ellington, A. D. *Nat. Nanotechnol.* **2016**, *11*, 157−163.
(21) Zhang, C.-H.; Tang, Y.; Sheng, Y.-Y.; Wang, H.; Wu, Z.; Jiang, J.-H. *Chem. Commun.* **2016**, *52*, 13584−13587.
(22) Bi, S.; Yue, S.; Wu, Q.; Ye, J. *Chem. Commun.* **2016**, *52*, 5455−5458.
(23) Wei, Y.; Zhou, W.; Li, X.; Chai, Y.; Yuan, R.; Xiang, Y. *Biosens. Bioelectron.* **2016**, *77*, 416−420.
(24) Wu, N.; Bao, L.; Ding, L.; Ju, H. *Angew. Chem., Int. Ed.* **2016**, *55*, 5220−5224.
(25) Asangani, I. A.; Rasheed, S. A. K.; Nikolova, D. A.; Leupold, J. H.; Colburn, N. H.; Post, S.; Allgayer, H. *Oncogene* **2008**, *27*, 2128−2136.
(26) Wu, S. W.; Peng, L.; You, M.; Han, D.; Chen, T.; Williams, K. R.; Yang, C. J.; Tan, W. *Int. J. Mol. Imaging* **2012**, *2012*, 1.
(27) Seferos, D. S.; Giljohann, D. A.; Hill, H. D.; Prigodich, A. E.; Mirkin, C. A. *J. Am. Chem. Soc.* **2007**, *129*, 15477−15479.
(28) Halo, T. L.; McMahon, K. M.; Angeloni, N. L.; Xu, Y.; Wang, W.; Chinen, A. B.; Malin, D.; Strekalova, E.; Cryns, V. L.; Cheng, C.; Mirkin, C. A.; Thaxton, C. S. *Proc. Natl. Acad. Sci. U. S. A.* **2014**, *111*, 17104−17109.
(29) Chinen, A. B.; Guan, C. M.; Ferrer, J. R.; Barnaby, S. N.; Merkel, T. J.; Mirkin, C. A. *Chem. Rev.* **2015**, *115*, 10530−10574.
(30) Keefe, A. D.; Pai, S.; Ellington, A. *Nat. Rev. Drug Discovery* **2010**, *9*, 537−550.
(31) Ferreira, C. S. M.; Cheung, M. C.; Missailidis, S.; Bisland, S.; Gariépy, J. *Nucleic Acids Res.* **2009**, *37*, 866−876.
(32) Punjabi, A.; Wu, X.; Tokatli-Apollon, A.; El-Rifai, M.; Lee, H.; Zhang, Y.; Wang, C.; Liu, Z.; Chan, E. M.; Duan, C.; Han, G. *ACS Nano* **2014**, *8*, 10621−10630.
(33) Jung, C.; Ellington, A. D. *Acc. Chem. Res.* **2014**, *47*, 1825−1835.
(34) Zhang, D. Y.; Winfree, E. *J. Am. Chem. Soc.* **2009**, *131*, 17303−17314.
(35) Srinivas, N.; Ouldridge, T. E.; Šulc, P.; Schaeffer, J. M.; Yurke, B.; Louis, A. A.; Doye, J. P. K.; Winfree, E. *Nucleic Acids Res.* **2013**, *41*, 10641−10658.
(36) Olson, X.; Kotani, S.; Padilla, J. E.; Hallstrom, N.; Goltry, S.; Lee, J.; Yurke, B.; Hughes, W. L.; Graugnard, E. *ACS Synth. Biol.* **2017**, *6*, 84−93.
(37) Rodjanapanyakul, T.; Takabatake, F.; Abe, K.; Kawamata, I.; Nomura, S. M.; Murata, S. *Phys. Rev. E: Stat. Phys., Plasmas, Fluids, Relat. Interdiscip. Top.* **2018**, *97*, 052617.
(38) Janas, M. M.; Wang, B.; Harris, A. S.; Aguiar, M.; Shaffer, J. M.; Subrahmanyam, Y. V.B.K.; Behlke, M. A.; Wucherpfennig, K. W.; Gygi, S. P.; Gagnon, E.; Novina, C. D. *RNA* **2012**, *18*, 2041−2055.
(39) Krützfeldt, J.; Rajewsky, N.; Braich, R.; Rajeev, K. G.; Tuschl, T.; Manoharan, M.; Stoffel, M. *Nature* **2005**, *438*, 685−689.

DOI: 10.1021/acs.analchem.8b04661
Anal. Chem. 2019, 91, 3374−3381